versity of Western Australia and the Western Australia Department of Agriculture (Perth, Western Australia, in December 1993 and January 1994) and weighed with a Mettler AE50 balance that was accurate to 0.1 mg.
14. Male spiders copulate with paired structures (emboli) that are inserted through separate coiled ducts into the paired sperm storage organs (spermathecae) of the female. In *Latrodectus*, the tip of the male's embolus always breaks off during insertion and remains inside the spermathecae or coiled ducts (*19*). By counting broken emboli inside 23 nonvirgin females (collected near Perth, Western Australia, in January 1994), I determined that 30.4% (7/23) had received only one palpal insertion, 52.2% (12/23) had received two palpal insertions and so had mated with one or two males, and 17.4% (4/23) had received three palpal insertions and so had mated with at least two and possibly three males.
15. G. A. Parker, *Biol. Rev.* **45**, 525 (1970); B. Sillen-Tullberg, *Behav. Ecol. Sociobiol.* **9**, 283 (1981). The proportion of eggs fertilized by the N male (x) was $x = (a - c)/(b - c)$ where a is the proportion hatched in the NI or IN group, b is the proportion hatched in the NN group, and c is the proportion hatched in the II group. P_2 in the IN group equaled x, and P_2 in the NI group equaled $1 - x$.
16. When the spermathecae of field-collected females (n = 23) were dissected (*14*), a total of 43 emboli were discovered. Of these, the majority (40/43) were located inside the female spermathecae rather than in the coiled ducts, suggesting that most males ejaculate directly into the sperm storage organ. Ejaculates of second males might then mix randomly with sperm already in the spermatheca, which suggests that increased sperm transfer is the mechanism by which longer copulation durations result in increased paternity.
17. Female rejection behavior is distinct and readily observable. In interactions that led to a successful copulation, the female remained quiescent in the web during most of the male's courtship. In comparison, rejection behavior consisted of a female repeatedly hitting at a courting male with her front legs, causing the male to drop from the web on a dragline. The male usually returned to the web and resumed courtship after the first few displacements, but nonreceptive females continued this behavior until the male eventually ceased courtship completely and moved to the substrate below the web.
18. T. E. Christenson and K. C. Goist Jr., *Behav. Ecol. Sociobiol.* **5**, 87 (1979); F. Vollrath and G. A. Parker, *Nature* **360**, 156 (1992).
19. R. G. Breene and M. H. Sweet, *J. Arachnol.* **13**, 331 (1985); B. J. Kaston, *Trans. San Diego Soc. Nat. Hist.* **16**, 33 (1970); J. W. Abalos and E. C. Baez, *Psyche* **70**, 197 (1963); R. D. S. Bhatnagar and J. G. Rempel, *Can. J. Zool.* **40**, 465 (1962).
20. L. M. Forster, in *Commerce and the Spread of Pests and Disease Vectors*, M. Laird, Ed. (Praeger, New York, 1984), pp. 273–289.
21. J. Kavale, thesis, University of Otago, Dunedin, New Zealand (1986).
22. K. Ross and R. L. Smith, *J. Arachnol.* **7**, 69 (1979).
23. S. K. Sakaluk, *Science* **223**, 609 (1984); *Evolution* **40**, 584 (1986); N. Wedell, *ibid.* **45**, 1975 (1991); *ibid.* **47**, 1203 (1993); D. T. Gwynne, in *Arthropod Social Systems*, J. Choe and B. Crespi, Eds. (Princeton Univ. Press, Princeton, NJ, in press).
24. I thank my supervisor, D. T. Gwynne, for considerable discussion and comments on this work and manuscript; W. J. Andersen, S. T. Emlen, L. M. Forster, P. D. Lorch, A. C. Mason, and P. W. Sherman for comments on the project or earlier versions of the manuscript; an anonymous reviewer for valuable suggestions; and W. J. Bailey, I. Dadour, C. Thomas, B. York Main, the University of Western Australia, and the Western Australia Department of Agriculture for facilitating my fieldwork. Supported by Natural Sciences and Engineering Research Council of Canada (operating grant to D. T. Gwynne and a 1967 Science and Technology scholarship to M.C.B.A.).

14 August 1995; accepted 2 November 1995

Direct Observation of Protein Solvation and Discrete Disorder with Experimental Crystallographic Phases

F. Temple Burling, William I. Weis,* Kevin M. Flaherty, Axel T. Brünger*

A complete and accurate set of experimental crystallographic phases to a resolution of 1.8 angstroms was obtained for a 230-residue dimeric fragment of rat mannose-binding protein A with the use of multiwavelength anomalous dispersion (MAD) phasing. An accurate image of the crystal structure could thus be obtained without resort to phases calculated from a model. Partially reduced disulfide bonds, local disorder, and differences in the mobility of chemically equivalent molecules are apparent in the experimental electron density map. A solvation layer is visible that includes well-ordered sites of hydration around polar and charged protein atoms, as well as diffuse, partially disordered solvent shells around exposed hydrophobic groups. Because the experimental phases and the resulting electron density map are free from the influence of a model, they provide a stringent test of theoretical models of macromolecular solvation, motion, and conformational heterogeneity.

Solvation and motion play key roles in protein folding, stability, and function. Water molecules are integral components of folded proteins, and the differential preference of amino acids for the aqueous environment is the basis of the hydrophobic effect, which is thought to be an important driving force in protein folding (*1*). Hydration of residues that participate in protein-ligand interactions and macromolecular association is important in determining the thermodynamics of binding. Molecular motion and flexibility are also essential aspects of macromolecular function, particularly in the induced fit, flexible-to-rigid transitions and large-scale conformational changes that occur in many proteins (*2*).

X-ray diffraction data result from temporal and spatial averaging over a large number of molecules in the crystal lattice and therefore provide an averaged view of solvation and flexibility. At the resolution limits typical of macromolecular crystals, the structure is usually modeled by a single conformer together with discrete sites of hydration. Thermal fluctuations are approximated by isotropic, harmonic motions. These models provide an incomplete description of the crystal structure. For example, solvent molecules constitute a large volume of macromolecular crystals (*3*), but only a small fraction of the solvent, consisting of fully occupied hydration sites ("bound" or "ordered" water molecules), is modeled. The remaining solvent is disordered but not completely featureless (*4*, *5*). It is particularly difficult to describe regions containing disordered solvent, portions of the molecule that display large thermal fluctuations [likely anisotropic and possibly anharmonic (*6*)], and conformational variability, all of which appear at relatively low electron density levels because of averaging over the copies in the crystal.

The interpretation of low electron density levels is made difficult by the presence of model bias that arises when inaccurate or incomplete experimental phases are substituted or augmented by phases derived from a model. When a feature is included in the model used to calculate phases for electron density maps, it often appears in the maps whether or not it is correct (*7*). In addition to causing model bias, inclusion of incorrect features in refinement can produce a relatively low conventional R value [$R = \Sigma_h||F_{obs}(h)| - |F_{calc}(h)||/\Sigma_h|F_{obs}(h)|$], which measures the agreement between structure factor amplitudes ($|F_{calc}|$) calculated from the refined model and the observed amplitudes ($|F_{obs}|$) over all reflections h. Misinterpretation or overinterpretation of the diffraction data can be reduced by monitoring the cross-validated or free R value (*8*); reduction of the free R value indicates a meaningful improvement of the model, whereas changes in the model that increase the free R value are likely fitting noise in the data.

The final R and free R values of macromolecular models are much larger than would be predicted from the statistical error in the observed amplitudes, presumably because current refinement models do not provide adequate descriptions of solvation

F. T. Burling and A. T. Brünger, Howard Hughes Medical Institute and Department of Molecular Biophysics and Biochemistry, Yale University, New Haven, CT 06520, USA.
W. I. Weis and K. M. Flaherty, Department of Structural Biology, Stanford University, Stanford, CA 94305, USA.
*To whom correspondence should be addressed.

Table 1. Data statistics. The space group is $P2_12_12_1$, with unit-cell parameters a = 65.51 Å, b = 72.22 Å, and c = 45.04 Å. Bijvoet mates were measured an average of 3.6 times. Statistics are given for diffraction data between 50 and 1.8 Å resolution. Values in parentheses are for data in the range 1.84 to 1.80 Å.

Wavelength (Å)	Number of reflections	Completeness (%)	Signal* (%)	R_{sym}† (%)
λ_1 1.3860 (edge)	37,989	99.2 (97.0)	87.5 (64.3)	8.0 (15.8)
λ_2 1.3854 (peak)	38,055	99.3 (97.3)	87.9 (64.6)	8.0 (15.5)
λ_3 1.3849 (inflection)	38,051	99.3 (97.1)	89.4 (69.4)	7.9 (14.2)
λ_4 1.3565 (remote)	38,059	99.3 (98.1)	89.8 (71.0)	7.7 (13.6)

*Percentage of reflections with $I > 3\sigma(I)$. †$R_{sym} = \Sigma_h\Sigma_i|I_i(h) - \langle I(h)\rangle|/\Sigma_h\langle I(h)\rangle$, where $I_i(h)$ is the ith measurement and $\langle I(h)\rangle$ is the weighted mean of all measurements of $I(h)$.

and thermal motion (*5*, *9*). It is therefore desirable to obtain accurate experimental phases at high resolution that can be used to produce electron density maps free of model bias. Models can then be improved and validated by comparison with the experimental phases. The standard method of experimental phase determination, multiple isomorphous replacement (MIR), is inappropriate for this purpose because nonisomorphism between native and derivative crystals limits the accuracy of the phases to resolutions well short of the diffraction limit of the crystal. In contrast, the multiwavelength anomalous dispersion (MAD) phasing method permits accurate phasing to the measurable diffraction limit, because phases are obtained from the variation in anomalous scattering at different wavelengths from a single crystalline species (*10*).

We have obtained an accurate set of MAD phases for a crystal of the dimeric Yb^{3+}-substituted subtilisin fragment of mannose-binding protein A (sub–MBP-A) (*11*, *12*). A complete set of MAD data was measured to 1.8 Å resolution (*13*) (Tables 1 and 2). Two approaches were used to extract phases from these data. First, phases were obtained by the least-squares method (*10*, *14*) implemented in the MADLSQ program (*10*, *15*) (Tables 2 and 3). A limitation of the MADLSQ procedure is that it does not produce reliable figure-of-merit estimates for the phases (*16*). Therefore, a second, "probabilistic" approach was used to analyze the MAD data, which consists of computing phase probability distributions derived from lack-of-closure relations between the observed reflections at different wavelengths (Table 4) (*17*). The advantage of the probabilistic treatment is that the phase probability distributions and corresponding figures of merit incorporate the predicted errors of the anomalous scatterer model as well as those of the observed intensities (Table 5). Figure-of-merit weighted electron density maps obtained from the probabilistic treatment should therefore be a more accurate representation of the actual electron density distribution, although the phase centroids obtained from both methods are the same to within the estimated error $\langle\Delta(\Delta\phi)\rangle$ (Tables 3 and 5).

The resulting experimental electron density map is of exceptional quality (Fig. 1), as expected from the phasing statistics and the high figure of merit (Table 4). The map was used to correct the model of Ho^{3+}-substituted sub–MBP-A (*18*) for subsequent refinement against the observed structure factor amplitudes (*19*) (Table 6). Water molecules were placed in the experimental MAD electron density map with conservative criteria (*19*) for peak height, shape, and hydrogen-bonding distance (Fig. 1A). The high quality of the experimental phases is demonstrated by the low average phase difference with the model phases and the high correlation coefficient between experimental and calculated protein electron density (Table 6).

The experimental electron density map shows that one of the two disulfide bonds in sub–MBP-A (Cys^{128}–Cys^{217}) exists as a roughly equal mixture of oxidized and reduced states in both protomers (Fig. 1B). The decreased occupancy in the oxidized state of Cys^{217} is indicated by its lower electron density level compared with that of the Cys^{128} thiol group. In the reduced state, the Cys^{217} sulfhydryl group is capable of forming hydrogen bonds to one of two carbonyl oxygens, and the Cys^{128} sulfhydryl group can form a hydrogen bond to a third carbonyl oxygen (Fig. 1B). This feature has not been observed in previous high-resolution structures of MBP-A (*18*, *20*) and may be unique to this particular sample.

Although most regions of the molecule can be modeled well with conventional refinement methods (Fig. 1, A and B), other

Table 3. MAD phasing statistics: least-squares method [MADLSQ (*10*, *15*)]. The least-squares phasing and statistics were obtained with the MADSYS suite of programs (*29*).

	50 to 1.80 Å	1.88 to 1.80 Å
$R_{sym}(\lvert{}^{\circ}F_T\rvert)$*	0.069	0.126
$R_{sym}(\lvert{}^{\circ}F_A\rvert)$*	0.239	0.470
$\langle\Delta(\Delta\phi)\rangle$*	20.7°	35.2°
$\langle m_{lsq}\rangle$†	0.94	0.89

*$R_{sym}(|F|) = \Sigma_h\Sigma_i||F_i(h)| - \langle|F(h)|\rangle|/\Sigma_h\langle|F(h)|\rangle$, where $F_i(h)$ is the amplitude of the ith determination and $\langle|F(h)|\rangle$ is the weighted mean of all determinations of $|F(h)|$, $^{\circ}F_T$ is the structure factor due to normal scattering from all the atoms, $^{\circ}F_A$ is the structure factor due to normal scattering from Yb^{3+} only, $\Delta\phi$ is the phase difference between $^{\circ}F_T$ and $^{\circ}F_A$, and $\langle\Delta(\Delta\phi)\rangle$ is the mean difference between independent determinations of $\Delta\phi(h)$. Quantities do not include reflections with $m = 0$, where m is the figure of merit. †$\langle m_{lsq}\rangle$ is the mean figure of merit, and here includes 88 reflections with $m = 0$.

Table 2. MAD phasing statistics: anomalous diffraction ratios and refined scattering factors. Values for the observed anomalous diffraction ratios are $\langle\Delta|F|^2\rangle^{1/2}/\langle|F|^2\rangle^{1/2}$, where $\Delta|F|$ is the Bijvoet difference at one wavelength (diagonal elements) or the dispersive difference at the two wavelengths intersecting at an off-diagonal element. The differences between Bijvoet mates at each wavelength for centric reflections, which would be 0.00 for perfect data, are shown in parentheses and serve as an estimate of the noise in the anomalous signals. Scattering factors $\Delta f'$ and $\Delta f''$ were held fixed at their theoretical values (*28*) at the remote wavelength to provide an absolute reference scale. Scattering factors at the other wavelengths were refined. Shown are the values obtained by MADLSQ (*10*, *18*); the values obtained from X-PLOR (*17*) are equal to within 10%.

Wavelength	Observed diffraction ratios				Scattering factors (*e*)	
	Edge (λ_1)	Peak (λ_2)	Inflection (λ_3)	Remote (λ_4)	$\Delta f'$	$\Delta f''$
λ_1	0.132 (0.056)	0.072	0.105	0.098	−25.4	10.7
λ_2		0.249 (0.056)	0.078	0.080	−19.7	23.2
λ_3			0.188 (0.054)	0.057	−9.4	17.5
λ_4				0.116 (0.053)	−10.3	10.1

Table 4. MAD phasing statistics: probabilistic method [X-PLOR (*17*, *27*)].

	50 to 1.80 Å	1.88 to 1.80 Å
Phasing power*		
$\lambda_4 \rightarrow \lambda_1$	4.3	2.9
$\lambda_4 \rightarrow \lambda_{-1}$	7.7	5.3
$\lambda_4 \rightarrow \lambda_2$	4.7	3.3
$\lambda_4 \rightarrow \lambda_{-2}$	10.8	7.8
$\lambda_4 \rightarrow \lambda_3$	2.7	1.6
$\lambda_4 \rightarrow \lambda_{-3}$	8.8	6.1
$\lambda_4 \rightarrow \lambda_{-4}$	7.9	6.1
$\langle m_{prob}\rangle$†	0.91	0.80

*Phasing power $[\langle|F_{h_4} - F_{h_i}|^2\rangle/\int_\Phi P_{\lambda_4\rightarrow\lambda_i}(\phi)(||F_{\lambda_4}|e^{i\phi} + F_{h_i} - F_{h_4}| - |F_{\lambda_i}||)^2 d\phi]^{1/2}$ computed for individual lack-of-closure expressions between the reflections of the reference wavelength λ_4, its Friedel mate, and the Bijvoet pairs measured at the other wavelengths (*17*). †$\langle m_{prob}\rangle$ is the mean figure of merit.

portions of the structure show varying degrees of conformational variability and disorder. Multiconformer refinement (*21*) was used to model this variability. Motion of certain side chains is observed (Fig. 1C), whereas complete disorder is inferred from large variations of the members of the multiconformer ensemble and from the lack of electron density for the first two residues of protomer B and for several surface side chains. The conformational variability is more pronounced for the second protomer: It has higher temperature factors when refined as a single conformer, as well as larger root-mean-square differences among members of the multiconformer ensemble (Table 6). This variability may be attributable to the different number of crystal packing interactions made by the two protomers (44 residues of protomer A participate in lattice contacts, compared with 30 in protomer B). The introduction of multiconformer refinement slightly improved both R values and the phase accuracy of the model (Table 6). However, the resulting R values are still significantly larger than the predicted error of the observed amplitudes ($R \gg R_{sym}/2$) (Table 1).

Most of the difference between observed and calculated electron density (*22*) occurs in the solvent regions, whereas little difference is apparent within the protein (Fig. 2A). Thus, incomplete treatment of solvent appears to be a significant component of the error in the model. The difference electron density map is very similar to the experimental electron density map in the solvent regions (Fig. 2B). Moreover, the experimental electron density in the bulk solvent regions is virtually independent of the reference wavelength used for the lack-of-closure expressions and the map calculation (*17*). The similarity among these electron density maps in the bulk solvent regions suggests that the observed features are a consequence of the actual solvent distribution and are not caused by noise in the data. They represent a time-averaged image of the solvent distribution around the protein. Thus, our results provide evidence for the existence of a nonuniform solvent distribution around proteins, as proposed by Badger, Caspar, and colleagues (*4*) on the basis of similar features in potentially noisy (*22*) or model-biased ($|F_{obs}| - |F_{calc}|$) $\exp(i\phi_{calc})$ difference electron density maps.

Site-specific radial distribution functions of solvent electron density (*5*) were computed from the experimental electron density map. They indicate a well-defined solvation shell around hydrophilic and hydrophobic groups (Fig. 2, C to E). Specific sites of hydration were apparent around polar and charged groups at hydrogen-bonding distance (compare with Fig. 1A). A diffuse electron density layer was apparent at approximately van der Waals distance around hydrophobic groups. A marked example is a ringlike feature near the methyl groups of Leu^{203} in protomer A (Fig. 2B). The electron density around Leu^{203} in protomer A suggests a network of four to five partially disordered water molecules (*23*). The disorder is presumably attributable to the many possible placements of water molecules around hydrophobic groups, which undergo rapid motion as indicated by nuclear magnetic resonance experiments on proteins (*24*).

The experimental electron density map described here was computed without resort to model phases. The partially disordered solvent, multiple conformations,

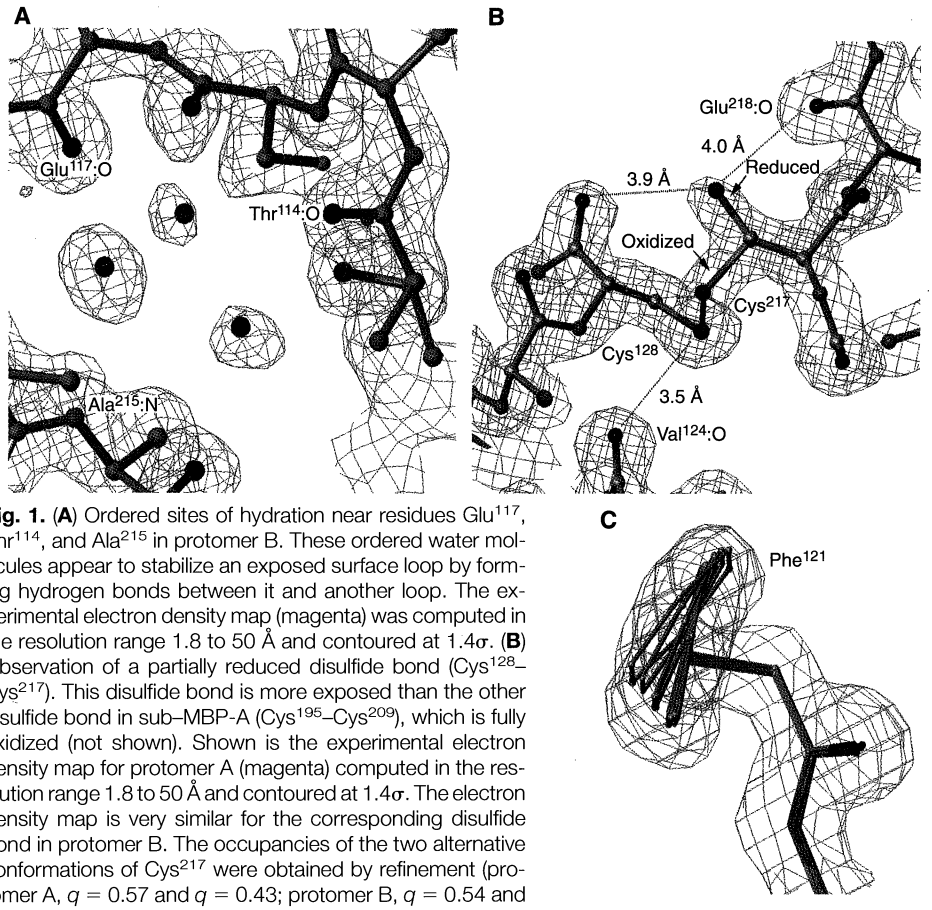

Fig. 1. (**A**) Ordered sites of hydration near residues Glu^{117}, Thr^{114}, and Ala^{215} in protomer B. These ordered water molecules appear to stabilize an exposed surface loop by forming hydrogen bonds between it and another loop. The experimental electron density map (magenta) was computed in the resolution range 1.8 to 50 Å and contoured at 1.4σ. (**B**) Observation of a partially reduced disulfide bond (Cys^{128}–Cys^{217}). This disulfide bond is more exposed than the other disulfide bond in sub–MBP-A (Cys^{195}–Cys^{209}), which is fully oxidized (not shown). Shown is the experimental electron density map for protomer A (magenta) computed in the resolution range 1.8 to 50 Å and contoured at 1.4σ. The electron density map is very similar for the corresponding disulfide bond in protomer B. The occupancies of the two alternative conformations of Cys^{217} were obtained by refinement (protomer A, $q = 0.57$ and $q = 0.43$; protomer B, $q = 0.54$ and $q = 0.46$, for the oxidized and reduced states, respectively). The sulfhydryl group of the alternative conformation of Cys^{217} can form hydrogen bonds with the carbonyl group of Glu^{218} or that of Cys^{128} (sulfur-oxygen distances are 4.0 and 3.9 Å for protomer A and 3.5 and 4.3 Å for protomer B, respectively). The sulfhydryl group of the reduced form of Cys^{128} can form a hydrogen bond with the carbonyl group of Val^{124} (distance is 3.5 Å in both protomers). The observed distances are within the range of observed cysteine-carbonyl hydrogen bonds (*30*). (**C**) Example of local conformational variability: wagging motion of Phe^{121} in protomer A. Multiconformer refinement (*21*) produces a family of conformers with considerable side-chain dihedral angle variability ($-172° < \chi_1 < -165°$, $54° < \chi_2 < 82°$) that fits the electron density better than does a refined single conformer ($\chi_1 = -168°$, $\chi_2 = 74°$). The experimental electron density map (magenta) is computed in the resolution range 1.8 to 50 Å and contoured at 1.4σ. Bonds and atoms are colored according to atom type (blue, N; red, O; tan, C; and green, S).

Table 5. MAD phasing statistics: comparison between least-squares and probabilistic methods.

	$\langle\lvert\phi_{lsq} - \phi_{prob}\rvert\rangle$*	$\langle\cos^{-1}(m_{lsq})\rangle$	$\langle\cos^{-1}(m_{prob})\rangle$
Strong anomalous data†	10.5°	5.1°	8.3°
Weak anomalous data‡	21.9°	11.4°	20.3°
All data	18.2°	9.3°	16.4°

*Mean phase difference between phases obtained from the least-squares method (ϕ_{lsq}) and the centroid phases obtained from the probabilistic method (ϕ'_{prob}), corrected for the contribution of the anomalous scatterer model. †The portion (32%) of the data with the strongest anomalous signal ($|\Delta F| = \|F^+| - |F^-\| > 2\sigma_{|\Delta F|}$ and $|F| > 2\sigma_{|F|}$). ‡Remaining 68% of the data.

and partially reduced disulfide bonds apparent in the map are therefore real features of the crystal structure and not an artifact of the refinement process. The experimental electron density map and the resulting solvent radial distribution functions thus serve as a stringent test of theoretical computer simulations of solvated proteins in a crystalline environment (*25*). Comparison of simulated solvent radial distribution functions around proteins (*25*) with those derived from the experimental map (Fig. 2, C to E) shows reasonable agreement around polar groups, but a somewhat broader distribution around hydrophobic groups is apparent in the experimental radial distribution function. The theoretical computer simulations may be improved by investigating this and other discrepancies between the simulations and the observed data, some of which may be attributable to crystallization conditions. Improved models of thermal motion, discrete disorder, and solvation for crystallographic refinement could be obtained by directly incorporating the experimental phase information into the refinement process to increase the observable-to-parameter ratio (*26*). Ultimately, these models could be used to obtain information about solvation, conformational variability, and motion in instances in which high-resolution experimental phase information is unavailable.

Table 6. Conventional (*19*) and multiconformer (*21*) refinement statistics. Statistics are for the resolution range of 10 to 1.8 Å.

	Conventional	Multiconformer
R value (%)	19.1	16.7
Free *R* value (*8, 19*) (%)	21.7	20.3
Bond length deviation (Å)	0.009	0.005
Bond angle deviation (degrees)	1.4	1.1
Improper angle deviation (degrees)	1.4	1.1
Residues in disallowed phi-psi regions (%)	0.5	0.6
Non-hydrogen protein atoms	1778	14,224
Water molecules ($B \leq 60$ Å^2)	159	159
NCS protomer A vs. B RMSD (residues 118 to 220) (Å)*	1.1 (0.56)	0.92 (0.48)
$\langle B \rangle$ for protomer A (Å^2)	13.3	8.1
$\langle B \rangle$ for protomer B (Å^2)	17.7	9.2
RMSD for protomer A (Å)†		0.58 (0.33)
RMSD for protomer B (Å)†		0.81 (0.58)
Mean phase difference (calc vs. exp) (degrees)‡	27.3	26.2
Map correlation coefficient for protomer A (calc vs. exp)§	0.92	0.93
Map correlation coefficient for protomer B (calc vs. exp)§	0.89	0.91

*Root-mean-square difference (RMSD) between corresponding atoms of the two protomers. Residues 109 to 117 were not included because the conformation differs markedly between the two protomers (*18*). Values in parentheses are for backbone atoms (N, C, C_α). †Average RMSD between each member of the multiconformer refinement (*21*) and the mean structure. Values in parentheses are for backbone atoms. ‡$\langle|\phi_{calc} - \phi_{obs}|\rangle$, where ϕ_{obs} is the centroid phase of the experimental phase probability distribution and ϕ_{calc} is the phase of the calculated structure factor F_{calc}. §$\langle\rho_{obs}\rho_{calc}\rangle/\sqrt{\langle\rho^2_{obs}\rangle\langle\rho^2_{calc}\rangle}$, where ρ_{obs} is the experimental electron density, ρ_{calc} is the calculated electron density, and the averages are taken over the volume of the indicated protomer.

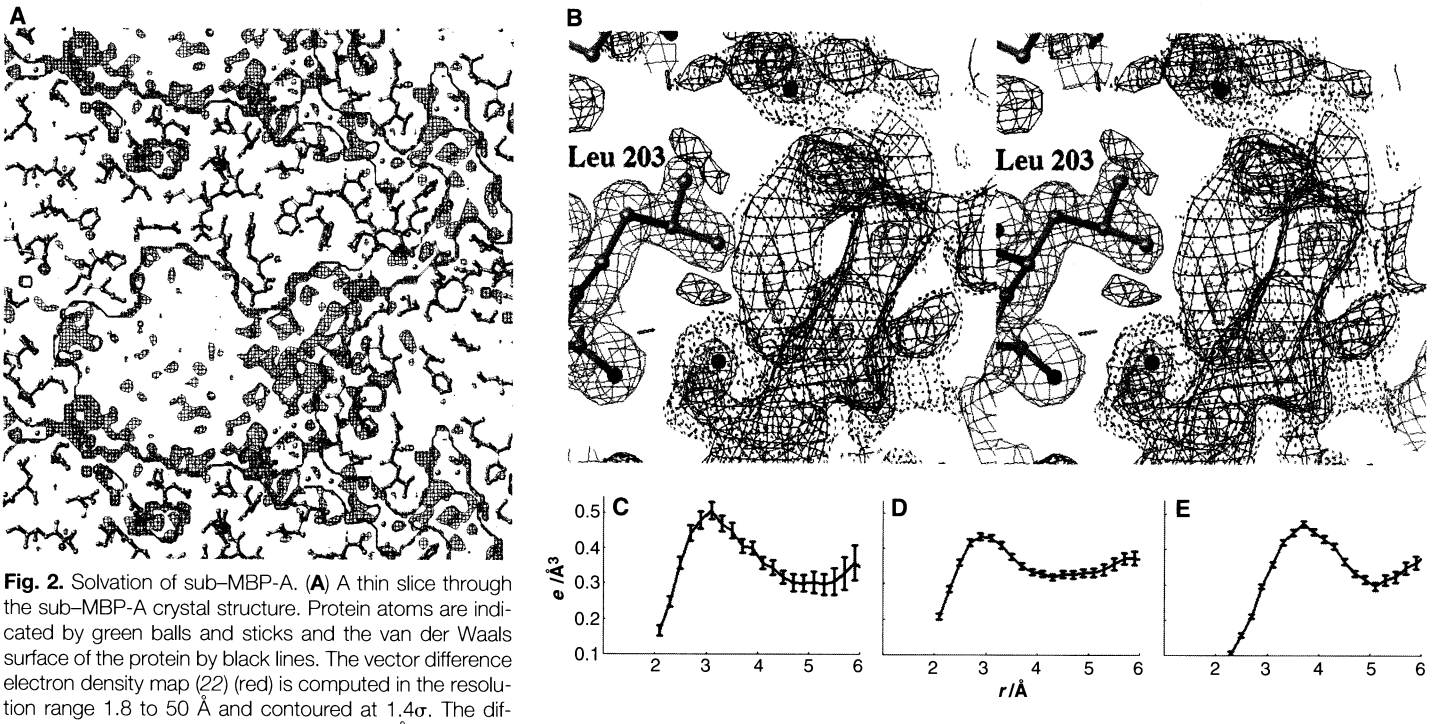

Fig. 2. Solvation of sub–MBP-A. (**A**) A thin slice through the sub–MBP-A crystal structure. Protein atoms are indicated by green balls and sticks and the van der Waals surface of the protein by black lines. The vector difference electron density map (*22*) (red) is computed in the resolution range 1.8 to 50 Å and contoured at 1.4σ. The diffraction data are virtually complete below 10 Å, and thus the observed features cannot be caused by truncation errors. (**B**) Stereo view of the solvent density around Leu^{203} in protomer A. The vector difference electron density map (*22*) is shown at 1.4σ (red), and the experimental electron density map at 1.4σ (magenta) and at 0.7σ (dashed black, with the density around the protein masked out for clarity). All maps are computed in the resolution range 1.8 to 50 Å. The difference map is very similar to the experimental map [the correlation coefficient (Table 6) between the two maps is 0.62 in the solvent regions and 0.02 in the protein regions]. The experimental map is largely independent of the reference wavelength used (the map correlation coefficients in the bulk solvent regions are ~0.9 between the experimental map computed with the reference wavelength λ_4 and those computed with wavelengths λ_1, λ_2, and λ_3). These high correlation coefficients preclude effects of uncorrelated noise in the observed amplitudes, but they do not exclude effects attributable to correlated (wavelength-independent) noise. However, correlated noise would produce erroneous difference electron density throughout the whole unit cell, including the protein, where little difference electron density is observed. (**C** to **E**) Radial distribution functions computed from the experimental map as described previously (*5*) in the resolution range 1.8 to 50 Å around ordered nitrogen (C), oxygen (D), and carbon (E) surface protein atoms; *r* is the distance between the averaged solvent electron density and the particular surface protein atoms. The radial distribution functions were placed on an approximate *e*/Å^3 scale by scaling the F_{obs} structure factor according to Wilson statistics and by adjusting the *F*(000) term such that the average electron density in the bulk solvent regions is equal to 0.333*e*/Å^3.

REFERENCES AND NOTES

1. M. Levitt and B. H. Park, *Structure* **1**, 223 (1993); E. Westhof, *Water and Biological Macromolecules* (CRC Press, Boca Raton, FL, 1993); B. T. Nall and K. A. Dill, *Conformations and Forces in Protein Folding* (American Association for the Advancement of Science, Washington, DC, 1991).
2. W. S. Bennett and R. Huber, *Crit. Rev. Biochem.* **15**, 291 (1985); G. E. Schulz, *Curr. Opin. Struct. Biol.* **1**, 883 (1991); M. Gerstein, A. Lesk, C. Chothia, *Biochemistry* **33**, 6739 (1994).
3. B. W. Matthews, *J. Mol. Biol.* **33**, 491 (1968).
4. J. Badger and D. L. D. Caspar, *Proc. Natl. Acad. Sci. U.S.A.* **88**, 622 (1991); J. Badger *et al.*, *Nature Struct. Biol.* **2**, 77 (1995).
5. J.-S. Jiang and A. T. Brünger, *J. Mol. Biol.* **243**, 100 (1994).
6. J. Kuriyan *et al.*, *ibid.* **190**, 227 (1986); T. Ichiye and M. Karplus, *Proteins Struct. Funct. Genet.* **2**, 236 (1987); *Biochemistry* **27**, 3487 (1988); W. Doster *et al.*, *Nature* **337**, 754 (1989); T. D. Romo *et al.*, *Proteins Struct. Funct. Genet.* **22**, 311 (1995).
7. A. Hodel, S.-H. Kim, A. T. Brünger, *Acta Crystallogr.* **A48**, 851 (1992).
8. A. T. Brünger, *Nature* **355**, 472 (1992).
9. F. T. Burling and A. T. Brünger, *Isr. J. Chem.* **34**, 165 (1994).
10. W. A. Hendrickson, *Science* **254**, 51 (1991).
11. W. I. Weis *et al.*, *J. Biol. Chem.* **266**, 20678 (1991).
12. The sub–MBP-A system was chosen for several reasons: (i) Crystals of lanthanide-substituted sub–MBP-A diffract well past 1.8 Å resolution (*11*). (ii) As shown by the original structure determination at 2.3 Å resolution with Ho^{3+}-substituted protein (*18*), the experimental phases were expected to be highly accurate because of the large contribution of two well-ordered Yb^{3+} per 115-residue protomer to the total scattering and the large anomalous scattering effects present at the lanthanide L_{III} edge. (iii) The dimer forms the asymmetric unit of the crystal (*11, 18*), providing two independent views of the protein in the crystal lattice.
13. Preparation of sub–MBP-A, cocrystallization with $YbCl_3$, and characterization of orthorhombic crystals were performed as described (*11*). Data were measured at beamline X4A at the National Synchrotron Light Source (Brookhaven, NY). A single crystal (0.35 mm by 0.1 mm by 0.1 mm) was serially transferred through solutions containing 15% polyethylene glycol 3350, 100 mM tris-HCl (pH 8.0), 10 mM NaCl, 2 mM $YbCl_3$, and 0, 5, 7.5, 10, and 15% 2-methyl-2,4-pentanediol as a cryoprotectant. The crystal was flash-cooled and maintained at ~110 K during data collection. An x-ray fluorescence scan of the crystal was taken after each fill of the synchrotron beam (total of four fills) and the monochromator was recalibrated to the absorption peak. Diffraction data were measured at four wavelengths chosen to optimize both Bijvoet and dispersive differences: λ_1, the absorption edge, corresponding to a minimum of the real part ($\Delta f'$) of the anomalous scattering factor for Yb^{3+}; λ_2, the absorption peak, corresponding to a maximum of the imaginary part ($\Delta f''$) of the anomalous scattering factor for Yb^{3+}; λ_3, the downward inflection of the L_{III} edge white line, corresponding to a maximum in $\Delta f'$; and λ_4, a high-energy remote wavelength, corresponding to a near maximal value of $\Delta f'$. Complete diffraction data were obtained from a single orientation by offsetting a major axis of the crystal from the spindle (to avoid a blind region) and collecting 65 consecutive 1.5° oscillation images. Each 1.5° sector of reciprocal space was measured at spindle settings ϕ and $\phi + 180°$, to collect Bijvoet mates at one wavelength, and repeated for each wavelength, so that eight images from each region were measured consecutively. The same region of reciprocal space was measured at different wavelengths during the same fill on the synchrotron ring to avoid potential systematic errors due to recalibration of the monochromator. Fuji imaging plates were scanned on a Fuji BAS2000 scanner. Profile-fit, Lorentz polarization–corrected intensities were obtained with the use of DENZO and SCALEPACK [Z. Otwinowski, *Proceedings of the CCP4 Study Weekend: Data Collection and Processing*, Warrington, UK, 29 and 30 January 1993, L. Sawyer, N. Isaacs, S. Bailey, Eds. (SERC Daresbury Laboratory, Warrington, UK, 1993), pp. 56–62]. Bijvoet mates were treated as independent observations for scaling and merging. Diffraction data for the four wavelengths were placed on a quasi-absolute scale, and the four data sets were scaled to one another with the CCP4 programs TRUNCATE and RSTATS [Collaborative Computing Project 4, *The CCP4 Suite: Programs for Protein Crystallography* (SERC Daresbury Laboratory, Warrington, UK, 1994)] for the MADLSQ calculations, and with X-PLOR (*27*) for the probabilistic calculations.
14. J. Karle, *Int. J. Quantum Chem. Symp.* **7**, 356 (1980).
15. Anisotropic scale factors were applied to the unmerged diffraction data to reduce noise in the Bijvoet and dispersive differences. The MADLSQ procedure was applied to the scaled and unmerged diffraction data. Redundantly determined amplitudes and phases were merged after the MADLSQ procedure (*10*).
16. A. Pähler, J. L. Smith, W. A. Hendrickson, *Acta Crystallogr.* **A46**, 537 (1990).
17. In contrast to the least-squares approach (*15*), the diffraction data were both scaled and merged before phasing, with Bijvoet mates treated as independent reflections. The high-energy remote wavelength λ_4 was chosen as the reference wavelength for phasing and for crystallographic refinement because it is the most complete set and has the lowest R_{sym} (Table 1). Observations of both Bijvoet mates at the four wavelengths are assumed to be statistically uncorrelated. The phase probability distribution $P_{\lambda_4}(\phi)$ for a particular reflection at wavelength λ_4 is thus given by a product of phase probability distributions,

$$P_{\lambda_4}(\phi) = P_{\lambda_4 \rightarrow \lambda_{-4}}(\phi) P_{\lambda_4 \rightarrow \lambda_3}(\phi) P_{\lambda_4 \rightarrow \lambda_{-3}}(\phi) \ldots \quad (1)$$

[J. C. Phillips and K. O. Hodgson, *Acta Crystallogr.* **A36**, 856 (1980)]. The phase probability distributions $P_{\lambda_i \rightarrow \lambda_j}(\phi)$ are obtained from lack-of-closure expressions,

$$P_{\lambda_i \rightarrow \lambda_j}(\phi) = \exp\left[- \frac{(\|F_{\lambda_i}| e^{i\phi} + F_{h_j} - F_{h_i}| - |F_{\lambda_j}|)^2}{2\sigma_{\lambda_i}^2 + 2\sigma_{\lambda_j}^2 + \epsilon E_{ij}^2} \right] \quad (2)$$

[T. C. Terwilliger and D. Eisenberg, *Acta Crystallogr.* **A43**, 6 (1987)], where $|F_{\lambda_i}|$ is the amplitude of the observed structure factor at wavelength i, σ_{λ_i} is the standard deviation of the amplitude at wavelength i, ϵ is a statistical weight, F_{h_i} is the wavelength-dependent component (dispersive and anomalous) to the structure factor of the anomalous scatterer centers at wavelength i, and E_{ij} is related to the error of the anomalous scatterer model. A negative sign in front of the wavelength number (λ_{-i}) indicates the Bijvoet mate of the particular reflection at wavelength i. E_{ij} can be estimated from the iterative relation

$$E_{ij} = 2 \left\langle \int_\phi P_{\lambda_i \rightarrow \lambda_j}(\phi) (\|F_{\lambda_i}| e^{i\phi} + F_{h_j} - F_{h_i}| - |F_{\lambda_j}|)^2 d\phi - \sigma_{\lambda_i}^2 - \sigma_{\lambda_j}^2 \right\rangle \quad (3)$$

where $P_{\lambda_i \rightarrow \lambda_j}(\phi)$ is given by Eq. 2 and the angular brackets denote an averaging over reflections in equal-volume resolution bins. The sharpness of the phase probability distribution $P_{\lambda_i \rightarrow \lambda_j}(\phi)$ is related to the magnitude of the $F_{h_j} - F_{h_i}$ vector; that is, the lack-of-closure expression depends simultaneously on both dispersive and anomalous differences, making the phase probability distributions less dependent on the choice of the reference wavelength than those obtained from a standard MIR approach [V. Ramakrishnan, J. T. Finch, V. Graziano, P. L. Lee, R. M. Sweet, *Nature* **362**, 219 (1993)]. Furthermore, the large anomalous signals present in the data (Table 2) result in a breakdown of the approximation in standard MIR treatments, so that the mean of the structure factor amplitudes of a Bijvoet pair does not equal the amplitude for the nonanomalous ("native") structure factor [$F_{native} \neq (|F^+| + |F^-|)/2$]. Use of separate lack-of-closure expressions for each Bijvoet mate between a reference wavelength and the others avoids this approximation. Detailed comparisons of the various methods will be presented elsewhere (A. T. Brünger, K. M. Flaherty, F. T. Burling, W. I. Weis, in preparation). Parameters of a model of the anomalous scatterer centers (positions, thermal factors, occupancies, and real and imaginary anomalous scattering factors of F_{h_i}) were refined by conjugate-gradient minimization against a maximum likelihood function,

$$R_{ML} = \sum_h 1/N \int_\phi P_{\lambda_4}(\phi) (\|F_{\lambda_4}| e^{i\phi} + F_{h_i} - F_{h_4}| - |F_{\lambda_i}|)^2 d\phi \quad (4)$$

[G. Bricogne, *Acta Crystallogr.* **A40**, 410 (1984); Z. Otwinowski, *Proceedings of the CCP4 Study Weekend*, Warrington, UK, 25 and 26 January 1991, W. Wolf, P. R. Evans, A. G. W. Leslie, Eds. (SERC Daresbury Laboratory, Warrington, UK, 1991, pp. 80–85]. This method is similar to the generation of phase probability distributions from the MADLSQ-derived wavelength-independent structure factors by the MADABCD procedure (*16*), in that Bijvoet and dispersive differences contribute to a lack-of-closure expression for each measured data point. It differs in two respects: (i) Phase probability distributions are obtained for structure factors at a reference wavelength, instead of the wavelength-independent structure factors derived from MADLSQ. (ii) The parameters of the anomalous scatterer model are refined in an iterative fashion with the maximum likelihood function R_{ML}, which makes the refinement more robust and the figures of merit more realistic. The experimental electron density map was computed with figure-of-merit weighted amplitudes at the reference wavelength λ_4 and centroid phases obtained from $P_{\lambda_4}(\phi)$ (Eq. 1). Centroid phases of $P_{\lambda_4}(\phi)$ were also used for phase difference calculations.
18. W. I. Weis, R. Kahn, R. Fourme, K. Drickamer, W. A. Hendrickson, *Science* **254**, 1608 (1991).
19. The previously determined Ho^{3+}-substituted sub–MBP-A structure refined at 2.3 Å resolution (*18*) served as an initial model for rigid-body refinement with X-PLOR (*27*). The program O [T. A. Jones, J. Y. Zou, S. W. Cowan, M. Kjeldgaard, *Acta Crystallogr.* **A47**, 110 (1991)] was used to make relatively minor corrections. One hundred fifty-nine ordered water positions were identified by selecting well-separated and approximately spherical peaks at 1.5σ above the average density of the experimental map with the protein masked out and within hydrogen-bonding distance to polar or charged atoms. Refinement made use of resolution-dependent weighting $1/\{1 - B_w[1/(2d) - 1/6]^2\}$ similar to that used in PROLSQ [W. A. Hendrickson, *Methods Enzymol.* **11**, 252 (1985)], where d denotes the Bragg spacing, and $B_w = 5.4$ was obtained by linear fit to the structure factor amplitudes versus d (W. I. Weis, unpublished data). This weighting scheme allows inclusion of low-angle reflections, which contain most of the information about solvent but which would otherwise dominate the refinement of the protein model. Overall B factor refinement, overall anisotropic B factor refinement, conjugate-gradient positional refinement, and a slow-cooling simulated annealing cycle [A. T. Brünger, A. Krukowski, J. Erickson, *Acta Crystallogr.* **A46**, 585 (1990)] were performed. The Yb^{3+} were held fixed during simulated annealing (to avoid excessive movements resulting from the large mass), which was followed by conjugate-gradient positional refinement, individual restrained B factor refinement, and refinement of the real ($\Delta f'$) and imaginary ($\Delta f''$) parts of the anomalous scattering factor of the Yb^{3+} chemical type. Geometric restraints used parameters previously described [R. A. Engh and R. Huber, *Acta Crystallogr.* **A47**, 392 (1991)]. The free R value was monitored with a test set containing a random selection of 6% of the diffraction data (the test set is defined such that both Friedel mates of a given reflection are included in the set). Noncrystallographic symmetry constraints or restraints were not imposed at any point in the refinement. The Cys^{217} sulfhydryl group was refined with two alternative conformations (Fig. 1B). All

refinements were performed with X-PLOR (*27*).
20. W. I. Weis, K. Drickamer, W. A. Hendrickson, *Nature* **360**, 127 (1992); W. I. Weis and K. Drickamer, *Structure* **2**, 1227 (1994).
21. Multiple conformers [J. Kuriyan *et al.*, *Proteins* **10**, 340 (1991)] (*9*) of the sub–MBP-A protein molecules were generated starting with the model that was obtained after single-conformer refinement (*19*). The water molecules and Yb^{3+} were restrained to their initial positions. Conformers of the protein were rendered invisible to each other in terms of chemical interactions. Each conformer in the ensemble contributed equally to the calculated structure factor with the occupancy set to the reciprocal of the number of conformers. Evaluation of the free *R* value as a function of the number of conformers produced a shallow minimum for eight conformers, which were used for subsequent analysis.
22. Vector difference electron density maps were computed by taking the vector difference between complex structure factors $[|F_{obs}| \exp(i\phi_{obs}) - |F_{calc}| \exp(i\phi_{calc})]$, the experimental structure factor with centroid phases obtained from $P_{\lambda 4}(\phi)$ (*17*) minus that computed from the refined single-conformer model. A conventional (model-phased) difference electron density map consisting of a Fourier synthesis of $(|F_{obs}| - |F_{calc}|) \exp(i\phi_{calc})$ is an approximation of the vector difference map [J. Drenth, *Principles of Protein X-ray Crystallography* (Springer-Verlag, New York, 1994), pp. 150–152]. As a consequence, vector difference maps of sub–MBP-A were observed to have less noise than conventional difference maps.
23. M. M. Teeter, *Proc. Natl. Acad. Sci. U.S.A.* **81**, 6014 (1984).
24. G. M. Clore *et al.*, *Structure* **2**, 89 (1994).
25. M. Levitt and R. Sharon, *Proc. Natl. Acad. Sci. U.S.A.* **85**, 7557 (1988); Y. Komeiji *et al.*, *Proteins* **16**, 268 (1993); M. Karplus and G. A. Petsko, *Nature* **347**, 631 (1990); P. J. Steinbach and B. R. Brooks, *Proc. Natl. Acad. Sci. U.S.A.* **90**, 9135 (1993); V. Lounnas *et al.*, *Biophys. J.* **66**, 601 (1994).
26. D. C. Rees and M. Lewis, *Acta Crystallogr.* **A39**, 94 (1983); E. Arnold and M. G. Rossmann, *ibid.* **A44**, 270 (1988); L. M. Rice and A. T. Brünger, *Proteins Struct. Funct. Genet.* **19**, 277 (1994).
27. A. T. Brünger, *X-PLOR. Version 3.1. A System for X-ray Crystallography and NMR* (Yale Univ. Press, New Haven, CT, 1992); developmental version of X-PLOR, available on request.
28. D. T. Cromer, *J. Appl. Crystallogr.* **16**, 437 (1983); ——— and D. L. Liberman, *J. Chem. Phys.* **53**, 1891 (1970).
29. W. A. Hendrickson and W. I. Weis, unpublished data.
30. L. M. Gregoret, S. D. Rader, R. J. Fletterick, F. E. Cohen, *Proteins Struct. Funct. Genet.* **9**, 99 (1991).
31. We thank P. Gros for assistance in designing the X-PLOR crystallographic language for phasing; V. Agrawal, S. Shah, and M. Willis for help with data collection; C. Ogata for beamline support; and P. Adams, M. Gerstein, M. Levitt, and L. Rice for critical reading of the manuscript. The coordinates and the diffraction data have been deposited with the Brookhaven Data Bank (accession number 1YTT). Supported by the Howard Hughes Medical Institute (A.T.B.), NSF (DIR9021975, A.T.B.), and NIH (GM50565, W.I.W.). W.I.W. is a Pew Scholar in the Biomedical Sciences.

8 September 1995; accepted 1 November 1995

Temporal Processing Deficits of Language-Learning Impaired Children Ameliorated by Training

Michael M. Merzenich,* William M. Jenkins, Paul Johnston, Christoph Schreiner, Steven L. Miller, Paula Tallal

Children with language-based learning impairments (LLIs) have major deficits in their recognition of some rapidly successive phonetic elements and nonspeech sound stimuli. In the current study, LLI children were engaged in adaptive training exercises mounted as computer "games" designed to drive improvements in their "temporal processing" skills. With 8 to 16 hours of training during a 20-day period, LLI children improved markedly in their abilities to recognize brief and fast sequences of nonspeech and speech stimuli.

Experiments conducted in human (*1*) and monkey (*2*) neurological models of perceptual learning have demonstrated that the capacity for segmentation of successive events in sensory input streams can be sharpened, apparently throughout life, by practice. Electrophysiological studies of learning-induced plasticity conducted in the neocortices of monkeys have provided a growing body of evidence about the neural processes that underlie practice-based improvements in both temporal segmentation and spectral (spatial) discrimination performances (*3–5*). These studies have shown that the ability of an adult animal to make fine distinctions about the temporal or spectral features of complex inputs can be sharply improved, or degraded, by a period of intensive behavioral training (*2–4*, *6*).

In parallel with animal and human models of temporal sequence learning, earlier studies of the receptive deficits of LLI children (*7*) had shown that they have a "temporal processing deficit" expressed by limited abilities at identifying some brief phonetic elements presented in specific speech contexts and by poor performances at identifying or sequencing short-duration acoustic stimuli presented in rapid succession (*8*). Consistent with a temporal processing deficit hypothesis, LLI children can distinguish these brief speech features and can correctly reconstruct stimulus input sequences if stimuli are presented in slower forms or at slower event rates (*8*).

Taken together, these experimental findings led us to hypothesize that the deficits underlying the phonetic reception limitations of a LLI child might arise in early life as a consequence of abnormal perceptual learning that then contributes to abnormal language learning (*3*, *4*). For example, a child might simply make more-limited-than-normal use of temporal information as he or she learns to make distinctions about speech inputs as a learning alternative, or a child might generate a representation of phonetic information under early childhood conditions (for example, in the presence of middle ear disease) under which acoustic inputs are consistently muffled. Cortical plasticity studies indicate that temporal processing deficits like those that emerge in LLI children would be expected from these learning scenarios, if they were to be undertaken in a training regime applied in a monkey model (*3*, *4*).

Visual psychophysical studies have already shown that very great improvements in the recognition of brief, successively presented stimuli can be achieved with practice in adult humans (*1*). In this study, we asked: Can we substantially alter the deficient temporal processing capacities of young, school-age LLI children by similar acoustic practice?

For training tools, we produced two audiovisual (AV) "games" designed around a circus theme to engage 5- to 10-year-old children at high levels of attention and enthusiasm within highly repetitive learning tasks. The first AV game (Circus Sequence) was a perceptual identification task in which a correct response in the exercise was a faithful reproduction of the order of two-stimuli sound sequences by touch-screen button-press sequences (*9*). The nonverbal stimuli applied in training were 16 octave-per-second upward- or downward-gliding (U and D, respectively) frequency-modulated (FM) tonal pairs (U-U, U-D, D-U, or D-D). Stimuli in each FM pair swept across the same frequency range. These stimuli were in the range of sweep frequencies and speeds that apply for the formant transitions of English consonants that LLI children have difficulty recognizing (*7*, *8*). The interstimulus intervals (ISIs) and FM frequencies were adaptive parameters.

The second game was a phonetic element recognition exercise implemented as a two-alternative forced-choice task in which the child was presented two consonant-

M. M. Merzenich, W. M. Jenkins, P. Johnston, C. Schreiner, W. M. Keck Center for Integrative Neurosciences and Coleman Laboratory, University of California, San Francisco, CA 94143–0732, USA.
S. L. Miller and P. Tallal, Center for Molecular and Behavioral Neuroscience, Rutgers University, 197 University Avenue, Newark, NJ 07102, USA.
*To whom correspondence should be addressed.